Quantifying the single scattering albedo for the January 2017 Chile wildfires from simulations of the OMI absorbing aerosol index

Jiyunting Sun[1,2], J. Pepijn Veefkind[1,2], Peter van Velthoven[1], Pieternel F. Levelt[1,2]

[1]Royal Netherlands Meteorological Institute, De Bilt, 3731 GA, the Netherlands

5 [2]Department of Geoscience and Remote Sensing (GRS), Civil Engineering and Geosciences, Delft University of Technology, Delft, 2628 CD, the Netherlands

Correspondence to: Jiyunting Sun (jiyunting.sun@knmi.nl)

Abstract. The absorbing aerosol index (AAI) is a qualitative parameter directly calculated from satellite measured reflectances. Its sensitivity to absorption by aerosol particles in combination with a long data record start in the late 1970's

10 makes it an important parameter for climate research. In the first part of this study, a series of AAI sensitivity analyses is presented exclusively on biomass burning aerosols. Later on, this study applies a radiative transfer model (DISAMAR) to simulate the AAI measured by the Ozone Monitoring Instrument (OMI) in order to derive the aerosol single scattering albedo (ω_0). The inputs for the radiative transfer calculations are satellite measurement geometry and surface conditions from OMI, aerosol optical thickness (τ) from the MODerate-resolution Imaging Spectroradiometer (MODIS), and aerosol micro-

15 physical parameters from the AErosol RObotic NETwork (AERONET), respectively. This approach is applied to the Chile wildfires for the period from 26 to 30 January 2017, when the OMI observed AAI of this event reached its peak. The Cloud and Aerosol Lidar with Orthogonal Polarization (CALIOP) failed to capture the complete evolution of the smoke plume, therefore the aerosol profile is parameterized. The simulated plume ascends to an altitude of 4.5-4.9 km, which is in good agreement with available CALIOP backscatter coefficient measurements. Due to the heterogeneity of the data that may

20 contain the pixels outside the plume, an outlier detection criterion has to be applied. The results show that the AAI simulated by DISAMAR is consistent with observations. The correlation coefficients fall into the range between 0.85 and 0.95. The retrieved mean ω_0 at 550 nm for the entire plume over the period from 26-30 January 2017 varies from 0.81 to 0.87, whereas the nearest AERONET station reported values in the range from 0.89 to 0.92. The difference in geolocation of the AERONET site and the plume, the assumption of homogeneous and static plume properties, the lack of the aerosol profile

25 information, and the uncertainties in the inputs for radiative transfer calculation are primarily responsible for this discrepancy.

1 Introduction

Biomass burning aerosols are generated from combustion of carbon-containing fuels, either by natural or anthropogenic processes (Bond et al., 2004; IPCC, 2014). They are of great concern from the perspective of climate (Kaufman and

30 Boucher, 2002; IPCC, 2007; Koch and Del Genio, 2010; Huang et al., 2013; IPCC, 2014). The reported radiative forcing of black carbon (BC) produced by fossil fuel and biofuel is around 0.4 Wm^{-2} (0.05 – 0.80 Wm^{-2}) (Ramanathan and Carmichael, 2008; Bond et al., 2013; Huang et al., 2013), but this estimate is highly uncertain. Accurate measurements of the aerosol single scattering albedo (ω_0) on a global scale can reduce the uncertainty in radiative forcing assessments (Hu et al., 2007). ω_0 is defined as the ratio of the aerosol scattering over the extinction. Currently ω_0 is mainly measured by ground-based

35 instruments (Dubovik et al., 1998; Eck et al., 2003; Petters et al., 2003; Kassianov et al., 2005; Corr et al., 2009; Yin et al., 2015). Satellite sensors, such as the POLarization and Directionality of the Earth's Reflectances (POLDER), can retrieve ω_0 from a combination of multi-angular, multi-spectral observations of the polarized radiation. By measuring the anisotropy of the reflected radiance for each ground pixel, POLDER is expected to determine the reflected solar flux more accurately (Leroy et al., 1997). Unfortunately, there is no continuous temporal coverage because the first two POLDER missions ended

40   prematurely due to technical problems on the satellite level. The third POLDER mission only covered the period 2004-2014. Instead, satellite derived ω_0 is usually retrieved simultaneously with the aerosol optical thickness (τ) based on the pre-defined aerosol properties, such as the near-UV aerosol product (OMAERUV) of the Ozone Monitoring Instrument (OMI) (Torres et al., 2005; Torres et al., 2007). But this aerosol absorption over near-UV is highly sensitive to the assumption on aerosol layer height. Satheesh et al. (2009) therefore used the τ from MODerate-resolution Imaging Spectroradiometer (MODIS), which is

45   independent of aerosol layer height, to constrain the OMAERUV retrieval. The validation showed that compared with operational OMAERUV algorithm, the retrieved aerosol height by the hybrid method is in a better agreement with air-borne measurements, implying a potential improvement in aerosol absorption retrieval. This OMI-MODIS joint retrieval was also evaluated by Gassó and Torres (2016). They found under less absorbing condition, the hybrid method is sensitive to the variations in the input τ, which is used to select the retrieved pair of aerosol layer and ω_0.

50   Herman et al. (1997) first defined the near Ultra-Violet (UV) absorbing aerosol index (AAI), which provides an alternative methodology to retrieve ω_0 from satellite observations. The near-UV AAI, usually derived from the spectral range between 340 and 390 nm, is a qualitative measure of absorbing aerosols that was first provided by the Total Ozone Mapping Spectrometer (TOMS) on-board Nimbus-7 in 1979. Since then several instruments have contributed to the AAI data record, that now spans nearly four decades. This long data record is an important motivation for us to improve methods to derive

55   quantitative aerosol information from the near-UV.

The most important advantage of the satellite retrieved AAI is that it does not dependent on assumptions on aerosol types, while a-prior aerosol types are major uncertainties in aerosol parameter retrievals, such as τ. Ginoux et al. (2004) suggested that comparing model simulations with AAI from TOMS allows a better control of discrepancies because the only error source is the model. Further advantages of AAI are the low reflectivity of the Earth's surface and the absence of significant

60   molecular absorption over the near-UV range. Using this band can ensure the aerosol absorption is one of the major contributors to the total signal. Moreover, the near-UV AAI is by definition highly sensitive to ω_0. Previous studies have proven the potential of the near-UV AAI from TOMS in aerosol properties retrieval. Torres et al. (1998) provided the theoretical basis of an inversion method to derive τ and ω_0 from backscattered radiation. This method was validated by ground-based observations during the Southern African Regional Science Initiative (SAFARI) 2000 measurement campaign.

65   The agreement of τ and ω_0 reaches $\pm 30\%$ and ± 0.03, respectively (Torres et al., 2005). Hu et al. (2007) retrieved global columnar ω_0 based on the AAI from TOMS with an average uncertainty of 15%.

This study is inspired by previous research to quantify the aerosol absorption from AAI. We use the near-UV AAI provided by OMI on-board Aura, the successor of TOMS, to derive the aerosol properties of the Chile wildfires in January 2017. Triggered by a combination of long-term drought and high temperature, this series of fires occurring in central Chile

70   (Pichilemu 34.39°S, 72.00°W and Consititución 35.33°S, 72.42°W) was regarded as the worst wildfire season in the national history (The Guardian, 2017). The fires led to evacuations of the affected areas and caused massive losses of the local forestry industry (pine and eucalyptus forests) (NASA.gov, 2017). The smoke plume was transported away from the source regions towards the tropical area in the Pacific Ocean by north-westward winds (Fig.1). In this study, we quantitatively retrieve the ω_0 of this smoke by simulating the near-UV AAI from OMI with the radiative transfer model Determining

75   Instrument Specifications and Analysing Methods for Atmospheric Retrieval (DISAMAR). The aerosol inputs of DISAMAR includes the τ retrieved from MODIS on-board the NASA EOS Aqua satellite, and information on aerosol micro-physical parameters provided by AERONET. In the next section, we provide a brief introduction on the near-UV AAI and its sensitivity to various parameters. The retrieval methodology is described in section 3. In section 4, retrieved results and uncertainty analysis of Chile 2017 wildfires are discussed, followed by main conclusions in section 5.

2 AAI sensitivity studies based on DISAMAR

In this section, we first introduce the near-UV AAI. In the sensitivity analysis, we show that the AAI depends not only on aerosol parameters, but also on the surface conditions and the observation geometry. The sensitivity analysis in this study is only designed for biomass burning aerosols.

2.1 Near-UV AAI definition

The concept of the near-UV AAI was first conceived to detect UV-absorbing aerosols from the spectral contrast provided by TOMS observations, known as the residue method (Herman et al., 1997). The basic idea of the residue method is that in a pure Rayleigh atmosphere, the reflectance (or equivalently the radiance (I_λ)) decreases strongly with the wavelength. The presence of absorbing aerosols will reduce this spectral dependency of I_λ. The change in this wavelength dependency is summarized as the AAI, which is calculated from the I_λ at the wavelength pair λ_1 and λ_2 ($\lambda_1 < \lambda_2$):

$$\text{AAI} = -100 \left(log_{10} \left(\frac{I_{\lambda 1}}{I_{\lambda 2}} \right)^{obs} - log_{10} \left(\frac{I_{\lambda 1}}{I_{\lambda 2}} \right)^{Ray} \right), \qquad (1)$$

The *obs* and *Ray* denote the I_λ from the satellite measurement and calculated using a Rayleigh atmosphere, respectively. The longer wavelength λ_2 is treated as reference wavelength where the surface albedo (a_s) is determined by fitting the observed radiance, i.e. $I_{\lambda 2}^{Ray}(a_s) = I_{\lambda 2}^{obs}$. This is done using an atmosphere containing only molecular scattering bounded by a Lambertian surface. The spectral dependence of the surface albedo is neglected thus $I_{\lambda 1}^{Ray}$ is calculated using the same value for a_s. Defining $\Delta I_{\lambda 1} = I_{\lambda 1}^{Ray} - I_{\lambda 1}^{obs}$, Eq.(1) can be rewritten as:

$$\text{AAI} = 100 log_{10} \left(\frac{\Delta I_{\lambda 1}}{I_{\lambda 1}^{obs}} + 1 \right) \qquad (2)$$

It is advantageous to use Eq.(2) because the AAI can be simply interpreted as the ratio between the simulated and observed radiance at λ_1.

2.2 Near-UV AAI sensitivity studies

In this section, we present results from sensitivity studies performed with the radiative transfer model DISAMAR. DISAMAR can perform simulations of the forward I_λ spectrum in a wide spectral coverage (270 nm to 2.4 μm) and models scattering and absorption by gases, aerosols and clouds, as well as reflection by the surface (De Haan, 2011). It uses either the Doubling-Adding method or the Layer Based Orders of Scattering (LABOS) for the radiative transfer calculations. In this study the latter one is used, because it is less computationally intensive (De Haan et al., 1987; De Haan, 2011). DISAMAR allows to apply several aerosol scattering approximations. Here we assume Mie scattering aerosols. The parameters to describe Mie particles and their corresponding values are listed in Table 1. Considering the Chile wildfires plumes, which were dominated by biomass burning aerosols, these sensitivity studies are specifically performed for parameterized smoke aerosols, with only fine mode particles and weak linearly wavelength dependency of the complex refractive index (n_r and n_i). The default values refer to observations of the daily average on January 27 of the AERONET station Santiago Beauchef (33.46°S, 70.66°W). We obtain the size distribution function and complex refractive index at 440, 675, 880 and 1018 nm from AERONET, and apply the linear interpolation / extrapolation to derive the complex refractive index over the spectrum from 340 to 675 nm, with spectral resolutions of 2 nm. Then DISAMAR uses above information to calculate the aerosol phase function P(Θ) and ω_0 over the full spectrum. The corresponding P(Θ) at 354 nm is presented in Fig.2. DISAMAR requires τ to be defined at reference wavelength 550 nm. Surface parameters include a spectrally flat a_s and the surface pressure P_s. The aerosol profile is parameterized as a single layer box shape, with its bottom at $z_{aer}-\Delta z/2$ and top at $z_{aer}+\Delta z/2$, where z_{aer} and Δz are the geometric central height and the geometric thickness of the aerosol layer, respectively. The whole sensitivity analysis is performed for cloud-free conditions. The wavelength pair of OMI (354 and

388 nm) is applied to compute the AAI. To make different sensitivities studies comparable, the AAI calculated in this section is normalized by the maximum value among each sensitivity study. Note that each sensitivity study always uses the default settings listed in Table 1 unless different values are explicitly mentioned.

Aerosol optical properties are determined by micro-physics, such as the real and imaginary part of the complex refractive index (n_r and n_i), and the particle size (r_g). Fig. 3 shows the variation of the AAI, $\Delta I_{\lambda 1}$, $I_{\lambda 1}^{obs}$ as well as of the optical properties ω_0 and the asymmetry factor g, as a function of the complex refractive and the particle size. The asymmetry factor g is the averaged cosine of the scattering angle Θ, weighted by $P(\Theta)$. Fig. 3 shows that the effect of the complex refractive index is dual. As shown in Fig.3 (a), an increase in the real part of refractive index n_r directly enhances the magnitude of $I_{\lambda 1}^{obs}$, whereas $\Delta I_{\lambda 1}$ reduces. This results in low values of the AAI, which correspond to a large ω_0 (Fig.3 (b)). Under the condition that measurement angle is $\Theta=150°$, the declining g implies that more light is scattered in the line-of-sight of the detector, thus the higher $I_{\lambda 1}^{obs}$. Conversely, the imaginary part of refractive index n_i, which is directly associated with ω_0, has an opposite influence, see Fig.3 (c) and (d). The particle size distribution has a more complicated influence on the AAI. As shown in Fig.3 (e), the AAI first decreases and then increases, when r_g is varied from 0.1 to 0.4 μm. The AAI primarily follows the behaviour of $\Delta I_{\lambda 1}$, whereas ω_0 is continuously decreasing and g is continuously increasing.

In addition to the micro-physics, the concentration and vertical distribution of aerosols also have a strong influence on the wavelength dependency of the radiance $\Delta I_{\lambda 1}$. As shown in Fig.4 (a), the AAI is positively correlated with τ. The AAI is highly sensitive to the aerosol vertical distribution (Herman et al., 1997; Torres et al., 1998; de Graaf et al., 2005). As the aerosol layer ascends (Fig.4 (b)), more molecular scattering beneath the aerosol layer is shielded, which reduces $I_{\lambda 1}^{obs}$ while increases $\Delta I_{\lambda 1}$. The relation between the AAI and z_{aer} is almost linear. Fig.4 (c) shows that at the same altitude, the AAI slightly increases with the geometrical thickness of the aerosol layer. The reason could be that a larger Δz indicates the coming sunlight has a higher possibility to be absorbed by aerosols, amplifying the absorption of the aerosol layer.

The calculated AAI does not only depend on the aerosols themselves, but also on ambient parameters such as surface and clouds. Although the near-UV AAI is capable to distinguish absorbing and non-absorbing agents (Herman et al., 1997) and even to retrieve aerosol information over clouds (Torres et al., 2012), the uncertainty triggered by clouds is relatively high and therefore cloudy conditions are excluded in this study. Surface conditions are parameterized by P_s and a_s. It can be seen in Fig.5 (a) that a decrease in P_s, or equivalently an elevated terrain height, leads to less Rayleigh scattering shielded between the surface and the aerosol layer. As a result, the AAI decreases significantly due to smaller $\Delta I_{\lambda 1}$, in agreement with a previous study (de Graaf et al., 2005). According to de Graaf et al. (2005), increasing a_s has two counteracting effects. On the one hand, it increases the amount of directly reflected radiation at the top of the atmosphere, namely a larger $I_{\lambda 1}^{obs}$, on the other hand it enhances the role of absorption by the aerosol layer rather than the surface, namely a larger $\Delta I_{\lambda 1}$. Which effect of a_s is decisive depends on P_s (Fig.5 (b)). When the aerosol layer is relative to the sea level (P_s = 1013 hPa), the first effect dominates. However, a brighter surface compensates the loss of molecular scattering shielded by the aerosols when the terrain height rises (P_s = 813 hPa), which makes the absorbing layer more detectable.

The AAI depends also on the Sun-satellite geometry. Here we provide the AAI as a function of the measurement geometries for the default case with the relative azimuth angle $\Delta \varphi = 180°$. As presented in Fig.6 (a), the AAI becomes very sensitive to the geometries for zenith angles larger than 60°, which confirms previous research (Herman et al., 1997; Torres et al., 1998; de Graaf et al., 2005). This is mainly due to the significant growth of $P(\Theta)$ when Θ becomes smaller (Fig.2). It is thus suggested that the OMI measurement with θ_0 larger than this value should be removed due to large variations in the AAI. To analyse the radiance behaviour as previously, we plotted the $I_{\lambda 1}^{obs}$ and $\Delta I_{\lambda 1}$ as a function of Θ along the cross section, respectively (Fig.6 (b)). It is noted that $I_{\lambda 1}^{obs}$ increases when Θ is larger than 90°, whereas the $P(\Theta)$ decreases at this range (Fig.2). The reason could be that the Rayleigh scattering has an increasing contribution to the radiance at those measurement angles (backscattering).

3 Methodology and datasets

In this section, we first present the datasets used and their pre-processing, followed by the strategy to retrieve the aerosol ω_0 while constraining the simulated near UV AAI to correspond to the observed one.

3.1 Datasets

3.1.1 OMI and GOME-2 absorbing aerosol index

The TOMS near-UV AAI retrieval has been proven a robust algorithm and applied to successive sensors, such as OMI on-board Aura and GOME-2 on-board MetOp-A/B. GOME-2 has higher spectral resolution (0.2-0.4 nm) than TOMS, but the spatial resolution is rather coarse (80×40 km^2). In this study, GOME-2 measured AAI at wavelength pair 340 and 380 nm (http://archive.eumetsat.int) is only used as an independent dataset to assess the potential bias of the OMI measurements. OMI combines advantages of both TOMS and GOME-2. It covers wavelengths from 264 to 504 nm with a spectral resolution of approximately 0.5 nm and has a much higher spatial resolution than GOME-2 of 13×24 km^2 (Levelt et al., 2006). Since OMI was launched in 2004, the AAI retrieved from this instrument has been widely used in various applications. Kaskaoutis et al. (2010) employed the OMI measured AAI for regional research of the aerosol temporal and spatial distribution in Greece. Torres et al. (2012) utilized the advantage of near-UV AAI to detect aerosols over clouds. The OMI observed AAI was even used to evaluate the impact of surface dust loading on human health (Deroubaix et al., 2013). Buchar et al. (2015) validated the NASA MERRA aerosol reanalysis with the AAI retrieved from OMI.

In this study, the OMI level 2 product OMAERO (https://disc.gsfc.nasa.gov) is used to provide AAI retrieved at the wavelength pair of 354 and 388 nm, and the corresponding viewing geometry and the surface condition when the measurements took place. The samples are included in the radiative transfer simulation only if θ_0 is smaller than 60°, and if ground pixels are not contaminated by sun-glint, clouds, row anomalies of the instrument, etc. The simulation is only applied to ground pixels inside the biomass burning plume, which as AAI values larger than 1, for both OMI and GOME-2.

3.1.2 MODIS and OMI aerosol optical thickness

MODIS on-board Aqua/Terra is a sensor that was specifically designed for atmosphere and climate research. The combination of two satellites ensures daily global coverage. The spatial resolution ranges from 250 m to 1 km and it has 36 spectral bands in the wavelength range between 400 nm and 14.4 μm (Remer et al., 2005). MODIS employs separated algorithms for aerosol retrieval over oceans and land, respectively (Tanré et al., 1997; Kaufman and Tanré, 1998; Hsu et al., 2004; Remer et al., 2005). Currently the τ provided by MODIS is one of the most reliable datasets (Lee et al., 2009), with an estimated uncertainty of only 3-5% over ocean and 5-15% over land (Remer st al., 2005). Besides, the MODIS retrieved τ is free from the uncertainty triggered by assumed aerosol profile (Satheesh et al., 2009). As mentioned before, DISAMAR requires τ at 550 nm. This study uses cloud-filtered τ at 550 nm from the Collection 6 level 2 product MYD04 as the input for radiative transfer calculation (https://ladsweb.modaps.eosdis.nasa.gov).

In addition, the τ measured by OMI and AERONET are treated as a reference dataset to evaluate potential biases in MODIS. The OMAERO retrieval uses multi-spectral fitting techniques. The retrieved τ is in good accordance with AERONET and is highly correlated with MODIS (Torres et al., 2007), with a correlation of 0.66 over land and 0.79 over the oceans (Curier et al., 2008), although it suffers from cloud contamination due to the relatively coarse spatial resolution of OMI. Due to the wavelength difference, the τ measured by OMI at 442 nm has to be transferred to 550 nm using the Ångström exponent (ÅE) $440 - 675$ nm taken from AERONET at the time when OMI flies over the selected site. The AERONET dataset used in this study is introduced in the next section.

3.1.3 AERONET aerosol properties

AERONET is an aerosol monitoring network of ground-based sun photometers. With standardized instruments, calibration, processing and distribution, AERONET provides a long-term global database for aerosol research and air-borne and space-borne measurement validation. The system takes two basic measurements. The τ and ÅE are retrieved from the direct solar irradiance measurements; the r_g, $P(\Theta)$ (Nakajima et al., 1983; Nakajima et al., 1996), ω_0 (Dubovik et al., 1998), n_r and n_i (Dubovik and King, 2000) are derived from multiple-angular measurements of sky radiance.

The AERONET site nearest to the fire sources of 2017 Chile wildfires is the Santiago Beauchef (33.46°S, 70.66°W) (https://aeronet.gsfc.nasa.gov). The dataset in use is version 2 level 1.5 product. To minimize the influence of temporal difference, the parameters of AERONET measured closest to the time of the OMI overpass of the site are used to simulate the optical properties of Mie scattering aerosols in DISAMAR. Note that the level 1.5 dataset is not quality-assured, and the location of this site is in downtown of Santiago City and close to major roads. The presence of scattering aerosols may bias the measurements of the plume.

The AERONET direct sun product provides τ and ω_0 are used to evaluate the MODIS τ and retrieved ω_0, respectively. The AERONET measured τ is transferred to 550 nm using the ÅE in range 440 – 675 nm while the ω_0 at 550 nm is linearly interpolated from values between 440 and 675 nm.

The AERONET inversion product needs to be processed into the inputs required by DISAMAR. Firstly, a conversion from the volume size distribution $V(r_v, \sigma_v)$ provided by AERONET to the number size distribution $N(r_g, \sigma_g)$ used in DISAMAR is required:

$$N(r_g, \sigma_g) = V(r_v, \sigma_v)\frac{3}{4\pi r_g^3}e^{-4.5\sigma_n^2} , \tag{4}$$

The following relation between the geometric and volumetric mean radii (r_g and r_v) and standard deviations (σ_g and σ_v) is assumed:

$$r_g = r_v e^{-3\sigma_g^2} , \tag{5}$$

$$\sigma_g = \sigma_v , \tag{6}$$

The fine and coarse mode particle size are derived by finding the two peaks of the log-normal distribution function provided by AERONET. The complex refractive index is assumed the same for both modes. Since bi-modal aerosol is not applicable in DISAMAR yet, we first calculate optical properties of two modes individually, then we externally combine the optical properties of two modes into a bi-modal aerosol with a fraction:

$$w_f = \frac{N_f(r_{g,f}, \sigma_{g,f})}{N_f(r_{g,f}, \sigma_{g,f}) + N_c(r_{g,c}, \sigma_{g,c})} , \tag{7}$$

$$w_c = 1 - w_f , \tag{8}$$

Then the weights for calculating the total ω_0 of the mixed aerosol are:

$$w_{\sigma,f} = \frac{w_f \sigma_f}{w_f \sigma_f + w_c \sigma_c} , \tag{9}$$

$$w_{\sigma,c} = 1 - w_{\sigma,f} , \tag{10}$$

Where the σ_f and σ_c are the extinction cross section of the fine and coarse aerosols. The expansion coefficients of the mixed aerosol is weighed by the ω_0 of the fine and coarse aerosols ($\omega_{0,f}$ and $\omega_{0,c}$), respectively:

$$w_{\omega_0,f} = \frac{w_f \sigma_f \omega_{0,f}}{w_f \sigma_f \omega_{0,f} + w_c \sigma_c \omega_{0,c}}, \tag{11}$$

$$w_{\omega_0,c} = 1 - w_{\omega_0,f}, \tag{12}$$

The spectral bands of the AERONET instrument at this site only cover the visible band. Due to the absence of observations, assumptions have to be made on the spectral dependence of aerosol properties to obtain their values in the near-UV band. The properties of biomass burning aerosol depend on the type of fuel, the procedure producing the smoke, the age of the smoke, and also the atmospheric conditions (Reid et al., 2005). Using measurements to constrain the input aerosol refractive index can reduce the uncertainties due to a-priori knowledge. Our treatment on the complex refractive index is as following: (1) take the complex refractive index at visible band (440 to 675 nm) from AERONET measurements; (2) linearly extrapolate the complex refractive index to near-UV band. The real part n_r for radiative transfer calculation is obtained in this step. A slight wavelength dependence of n_r is found from the measurements; (3) for the imaginary part n_i, we multiply it (for the entire wavelength from UV to visible) with a scaling factor as we set it as a free parameter. By varying the value of the scaling factor, both the magnitude and the wavelength dependence of n_i can change to meet the requirement of retrieval.

3.1.4 CALIOP backscattering coefficient

The CALIOP on-board CALIPSO, which was launched in 2006, provides high-resolution profiles of aerosols and clouds. It has three channels with one measuring the backscattering intensity at 1064 nm and the rest measuring orthogonally polarized components at 532 nm backscattering intensity (Winker and Omar, 2006). Due to the limited spatial coverage, CALIOP did not observe the Chile plume for all the cases for which we have OMI observations. We only use the total attenuated backscatter at 532 nm from level 1B Version 4.10 Standard data to evaluate the parameterized aerosol profiles (https://eosweb.larc.nasa.gov/project/calipso).

3.2 Methodology

In this study, we employ the radiative transfer model DISAMAR to simulate the near-UV AAI from OMI and to derive the ω_0 for a specific case, i.e. the Chile wildfires in January 2017. We select the period from 26 to 30 January 2017 (28 January is excluded due to lack of data) when the AAI value reached its peak.

The forward simulation consists of two major steps. First, DISAMR calculates the Mie aerosol optical properties with aerosol micro-physical information taken from AERONET measurements (r_g, n_r and n_i). As mentioned in Section 3.1.3, we set the spectral-dependent imaginary part n_i as a free parameter to vary ω_0. Then, DISAMAR operates radiative transfer calculation with the calculated aerosol optical properties for a specific aerosol and environmental conditions.

It is noted that the observed aerosol vertical profiles is limited for the Chile wildfires. Previous research suggested AAI cannot be quantitatively used without τ or z_{aer} information (Gassó and Torres, 2016). Instead, we implement the same parameterization as in the sensitivity study to obtain the aerosol profile. Since the AAI dependency on Δz is minor (Fig.4 (c)), and to reduce the computational cost, Δz is set constant of 2 km based on the information from the CALIOP measurements of backscattering coefficient (β) at 532 nm (Fig.7). The z_{aer}, to which the AAI is highly sensitive, is treated as an unknown variable to be retrieved together with ω_0.

Consequently, with various combinations of z_{aer} and n_i, a lookup table (LUT) of the calculated AAI is constructed with DISAMAR. It should be noted that for all ground pixels in the plume we assume the same aerosol microphysical properties as well as the same vertical profile. Pixels outside the plume may have had significantly different properties and this will affect the results. But as shown in Fig.8, the distribution of OMI measurements is sparse in space, which implies that the dataset is quite sensitive to geographical outliers that may cause the heterogeneous properties of the plume. Consequently, we apply a data quality control procedure before retrieving ω_0. First, we manually remove the pixels that are geographically isolated from the main plume. Furthermore, we remove the potential outliers based on statistical tool. We filter the dataset using an outlier detection based on the interquartile range (IQR) of the AAI difference between DISAMAR simulations and OMI measurements. According to Tukey's fences (Tukey, 1977), an AAI difference falling outside range between Q1-1.5 IQR and Q3+1.5 IQR may be regarded as an outlier and removed, where Q1 and Q3 are the first and third quartiles of the

275 AAI difference, and the IQR is the range between Q1 and Q3. Only the data passing the outlier detection criterion is used to calculate the cost function (Eq.(3)):

$$RMSE = \sqrt{\frac{\Sigma_i^n \left(AAI_{DSM,i}^{qualified} - AAI_{OMI,i} \right)^2}{n}} , \qquad (3)$$

Here AAI_i indicates the AAI for ith ground pixel of the selected OMI data; subscripts DSM and OMI indicate DISAMAR simulation and OMI observation, respectively. The combination of z_{aer} and ω_0 that leads to the minimum residue is used to
280 simulate the AAI.

Finally, the simulated AAI is compared with OMI observations. We also employ the independent data from GOME-2 on MetOp-A/B as a reference to identify the potential bias of OMI. Similarly, the τ retrieved from OMI and AERONET serves as a reference to that of MODIS. The estimated aerosol profile and ω_0 at 550 nm are evaluated with independent observations from CALIOP and AERONET, respectively.

285 **4 Results and discussion**

By applying the methodology described in the previous section, we quantitatively retrieved the aerosol profile and ω_0 of the Chile 2017 wildfires by AAI simulation. The OMI measurements of the plume are displayed in Fig.8 (a) – (d). The presented ground pixels are with AAI value larger than 1, and are free of cloud contamination, sun-glint and row anomaly of the instrument. Fortunately, the remaining data is still able to capture the main plume features. It can be clearly seen that from 26
290 to 30 January, the plume produced by wildfires in the central Chile was transported by the south-easterly trade wind from the continent towards the lower latitude region of the Pacific Ocean. The plume travelled over a distance of 3000 km during the period.

The vertical movement of the plume is given by CALIOP backscattering coefficient measurements (β) at 532 nm (Fig.7). The CALIOP paths closest to the plume are marked by a black dashed line in Fig.7. It is noted that CALIOP did not always
295 measure the plume and may even fail to capture the elevated plume, e.g. on 26 January. The aerosol layer captured by CALIOP is distributed from 2 km to 6 km, with an average height at approximately 4-5 km. The ascent of the plume was driven by the heat generated by the fires and sunlight absorption, as well as the atmospheric vertical motions.

Fig.8 (e) – (h) show the AAI simulation selected by the data quality control mentioned in Section 3.2. The spatial distribution of the simulated AAI shows similar patterns as the OMI observations. Some data points that are geographically
300 isolated from the plume, e.g. in case 26 and 30 January, differ strongly from what are observed inside the plume. Including these outliers in the optimization could bias the retrieved aerosol properties. This can also be seen in Fig.8 (i) – (l), where the points passing the data quality control described in Section 3.2 are highlighted in red color. By removing the outliers, the average spatial correlation coefficient reaches 0.90.

Table 2 lists the statistics of the qualified AAI data, in terms of the median, relative difference and RMSE. The median of
305 measured AAI ranges from 2 to 4 during the research period. Except 26 January, the median of simulated AAI in other cases is in good agreement with the measurements, with relative differences within $\pm6\%$. The low RMSE confirms the high spatial consistency between the simulations and the observations. The majority of the simulated AAI of 26 January is negatively biased, which is reflected by the small slope without an intercept correction in Fig.8 (i). A systematic bias in the inputs might cause this result. In terms of ω_0, both the AERONET measured and the AAI retrieved aerosol absorption become weaker
310 with time (Table 2). Although the simulated and observed AAI are in good agreement, the difference in ω_0 is significant. The mean of the retrieved ω_0 at 550 nm for the whole period is 0.84, contrast to the AERONET measurements with a mean value of 0.90.

There are many sources accounting for this discrepancy. First of all, the nearest site Santiago_Beauchef is not exactly in the primary biomass burning regions as mentioned in section 3.1.3. The AERONET site is located in downtown, where reflective urban or industrial aerosols may have been mixed with the smoke enhancing the ω_0. This would also affect the complex refractive index used in radiative transfer calculation, since we use the AERONET measured refractive index to constrain the forward simulations. According to Table 2, the retrieved n_i reveals that the difference between 354 and 388 nm is less than 5%. This small spectral dependence of n_i is mainly determined by AERONET measurements in the visible band (dashed lines), whereas the effect of the scaling factor is minor in this case (Fig.9). We thus find a much weaker wavelength dependence than in the Jethva and Torres (2011) study, where a 20% difference between the two UV wavelengths was applied to OMAERUV algorithm to achieve the result that 70% of the retrieved ω_0 differ less than ± 0.03 from the ω_0 from the AERONET measurements. A stronger spectral dependence of n_i between 354 and 388 nm would allow simulations to reach a higher AAI while keeping n_i at a relatively low level, so would retrieve a higher ω_0 at 550 nm. The presence of non-absorbing aerosols weakens the spectral dependence (particularly in the UV spectral range) and the linear extension would overestimate the aerosol absorption. In this situation, the uncertainties due to assumed spectral aerosol properties might compensate the measurement errors to some extent. Furthermore, the AERONET inversion product is not error-free. The uncertainty of size distribution retrieval is minor for biomass burning aerosols (Dubovik et al., 2000), but under optically thick circumstances, when retrievals are quality-assured, the reported accuracy of complex refractive index is 0.04 for n_r and 30%-50% for n_i, respectively (Dubovik et al., 2002). It is also reported that AERONET tends to underestimate the absorption of biomass burning aerosols compared with in situ measurements (Dubovik et al., 2002; Reid et al., 2004). The uncertainty of ω_0 is 0.03 under high aerosol loading ($\tau_{440} > 0.5$) and 0.05-0.07 under low aerosol loading (Dubovik et al., 2002; Holben et al., 2006).

Apart from AERONET itself, information from other datasets could also bias our estimate of aerosol absorption. Among all the inputs, the parameterization of a one-layer box-shape aerosol profile could be the largest error source. Although the influence of Δz on the AAI is small (Fig.4 (c)), the AAI calculation highly depends on z_{aer} (Fig.4 (b)). As shown in Table 2, the estimated plume altitude varies from 4.5 to 4.9 km. As the black solid line indicated in Fig.7, the retrieved z_{aer} can capture the measured geometric vertical location of the plume. The z_{aer} on 26 January seems overestimated because of the temporal and spatial difference. Concretely, CALIOP sampled the plume near the sources and close to the surface, while the plume observed by OMI had been already elevated and transported to the open ocean. The lack of information on the real plume height makes it challenging to determine whether the plume height is responsible for the systematic bias in Fig.8 (i). Except for 26 January, z_{aer} is in good agreement with what CALIOP observed. Although the retrieved aerosol profiles are convincing to some extent, one should keep in mind that CALIOP and OMI observations are not exactly co-located. Besides, the parameterized aerosol profile may fail to represent the spatial variation of the plume. Therefore, the uncertainty cannot be directly determined due to the lack of validation observations.

Among the four days for which we retrieved ω_0, the value for 27 January is significantly lower than others. For this day the agreement with CALIOP is reasonable and also the CALIOP track is not far away from the OMI measurement. We therefore explore the effect of measurement biases in AAI and τ on the retrieved ω_0. We investigate the potential bias of these two datasets by plotting the histogram of the AAI measurement difference between GOME-2 and OMI (Fig.10 (a)), against the τ measurement difference between MODIS and OMI (Fig.10 (b), both are converted into 550 nm). It is clear that on 27 January, the AAI from OMI seems to be overestimated compared to GOME-2. Although the difference in wavelength pair choice for AAI retrieval, measurement time and condition, etc., could contribute to the AAI discrepancy between GOME-2 and OMI, exploring the difference between the two datasets is beyond the scope of this study. In aspect of input aerosol concentration, the τ from MODIS could be potentially underestimated. Fitting a higher AAI with a lower input τ leads to an overestimation in aerosol absorption. Here, we analytically quantify the impact of τ for this specific case by systematically enhancing the τ of MODIS with a constant variation ($\Delta\tau$) added to all pixels, with the AAI level and the aerosol profile

remain unchanged. Fig.10 (c) presents how the AAI RMSE and the estimated ω_0 respond to the enhanced τ. It can be clearly seen that an increase in overall τ level by 0.07 raises ω_0 to 0.84 and optimizes the AAI simulation to a RMSE less than 0.45. If we apply this τ adaption, the retrieved ω_0 of 27 January becomes more consistent with the other days.

360 Apart from the observational errors in AERONET, OMI and MODIS data, the assumption that the plume features are homogeneous could also result in the discrepancy between AAI retrieved and AERONET measured ω_0. In reality, the plume altitude, the optical properties and even the chemical compositions could vary in space and time, while our simulations cannot take into account those effects.

5 Conclusions

Biomass burning is a major source of absorbing aerosols making a significant contribution to climate warming.
365 Quantitatively characterizing the absorption by biomass burning aerosols is therefore important to reduce the uncertainty in assessments of global radiative forcing. Facing the lack of long-term ω_0 records, this study explores an approach to retrieve ω_0 based on reflectivity in the near-UV channel measured by OMI. Although AAI is not a geophysical parameter and depends on many factors, its independence from pre-defined aerosol types, its high sensitivity to aerosol absorption as well as its long-term data record, makes it an attractive quantity to aerosol research.

370 We test the retrieval of ω_0 for the wildfires happening in central Chile in January 2017. After filtering the data from outliers, a high spatial correlation coefficients (0.85 to 0.95) reaches between the simulated and observed AAI. The retrieved aerosol profiles indicate the plume was elevated to height of 4.5-4.9 km during the research period. These results are in agreement with CALIOP measurements. This average of the retrieved ω_0 at 550 nm is approximately 0.84, which is 0.06 lower than that of AERONET retrieval. The retrieved ω_0 is out of the typical uncertainty in the ω_0 retrieved from AERONET ($\pm$0.03). The
375 sources for discrepancy includes: the location of the AERONET site that may bias the measured ω_0 and the spectral dependency of complex refractive index; the simplified parameterization of the aerosol profile; the observational errors in the input aerosol micro-physics, τ, as well as AAI; and the assumption of homogeneous and static plume properties, which ignores the plume evolution over space and time. We quantitatively analyze the uncertainty of τ for a specific case (27 January) when the estimated aerosol profile is in good agreement with the CALIOP measurements. An improvement in
380 retrieved ω_0 can be seen by adapting the magnitude of aerosol concentration.

This study proves the potential of utilizing OMI measured AAI to quantitatively characterize aerosol optical properties like ω_0. Currently, it is challenging to retrieve and validate results without reliable aerosol profile information. In the future, the availability of daily global aerosol profile data, e.g. the L2 aerosol layer height product TROPOspheric Monitoring Instrument on-board Sentinel-5 Precursor (TROPOMI) that is underdevelopment (Sanders and de Haan, 2016), are expected
385 to provide a stronger constraint on the forward calculation and to significantly reduce the uncertainty in the retrieved aerosol properties. Perhaps, more sophisticated assumptions on spectral-dependent aerosol absorption (e.g. steeper gradient of n_i in UV than visible band) have to be made and evaluated by other observational aerosol properties in UV spectral range, e.g. AERONET measured τ in UV band, instead of only depending on measured refractive index in visible band.

Acknowledgements

390 This work was performed in the framework of the KNMI Multi-Annual Strategic Research (MSO). The authors thank to NASA's GES-DISC, LAADS DAAC and ASDC for free online access of OMI, MODIS and CALIOP data. The authors also thank to the Centre for Climate Resilience Research (CR)2 at University of Chile (CONICYT/FONDAP/15110009) providing the data of the Santiago_Beauchef AERONET station.

References

395   Bond, T. C., Streets, D. G., Yarber, K. F., Nelson, S. M., Woo, J. H. and Klimont, Z.: A technology-based global inventory of black and organic carbon emissions from combustion, J. Geophys. Res. D Atmos., 109, D14203, doi:10.1029/2003JD003697, 2004.

Bond, T. C., Doherty, S. J., Fahey, D. W., Forster, P. M., Berntsen, T., Deangelo, B. J., Flanner, M. G., Ghan, S., K??rcher, B., Koch, D., Kinne, S., Kondo, Y., Quinn, P. K., Sarofim, M. C., Schultz, M. G., Schulz, M., Venkataraman, C., Zhang, H.,

400   Zhang, S., Bellouin, N., Guttikunda, S. K., Hopke, P. K., Jacobson, M. Z., Kaiser, J. W., Klimont, Z., Lohmann, U., Schwarz, J. P., Shindell, D., Storelvmo, T., Warren, S. G. and Zender, C. S.: Bounding the role of black carbon in the climate system: A scientific assessment, J. Geophys. Res. Atmos., 118, 5380–5552, doi:10.1002/jgrd.50171, 2013.

Buchard, V., Silva, A. M., Colarco, P. R., Darmenov, A., Randles, C. A., Govindaraju, R., Torres, O. and Goddard, N.: Using the OMI aerosol index and absorption aerosol optical depth to evaluate the NASA MERRA Aerosol Reanalysis,

405   Atmos. Chem. Phys., 15, 5743–5760, doi:10.5194/acp-15-5743-2015, 2015.

Corr, C. A., Krotkov, N., Madronich, S., Slusser, J. R., Holben, B., Gao, W., Flynn, J., Lefer, B., Kreidenweis, S. M., Collins, F., Sciences, E., County, B., Division, A. C., Resource, N., Collins, F., Branch, B. S. and Sciences, A.: Retrieval of aerosol single scattering albedo at ultraviolet wavelengths at the T1 site during MILAGRO, Atmos. Chem. Phys., 9, 5813–5827, 2009.

410   Curier, R. L., Veefkind, J. P., Braak, R., Veihelmann, B., Torres, O. and de Leeuw, G.: Retrieval of aerosol optical properties from OMI radiances using a multiwavelength algorithm: Application to western Europe, J. Geophys. Res. Atmos., 113, D17S90, doi:10.1029/2007JD008738, 2008.

Deroubaix, A., Martiny, N., Chiapello, I. and Marticorena, B.: Remote Sensing of Environment Suitability of OMI aerosol index to re fl ect mineral dust surface conditions : Preliminary application for studying the link with meningitis epidemics in

415   the Sahel, Remote Sens. Environ., 133, 116–127, doi:10.1016/j.rse.2013.02.009, 2013.

de Graaf, M., Stammes, P., Torres, O. and Koelemeijer, R. B. A.: Absorbing Aerosol Index: Sensitivity analysis, application to GOME and comparison with TOMS, J. Geophys. Res. D Atmos., 110, D01201, doi:10.1029/2004JD005178, 2005.

de Haan, J. F.: DISAMAR Algorithm description and background information, De Bilt, 2011.

de Haan, Johan F., Bosma, P.B and Hovenier, J. W.: The adding method for multiple scattering of polarized light, Astron.

420   Astrophys., 183, 371–391, 1987.

Dubovik, O., Holben, B., Eck, T. F., Smirnov, A., Kaufman, Y. J., King, M. D., Tanré, D., Slutsker, I., Sciences, G. E. and Directorate, E. S.: Variability of Absorption and Optical Properties of Key Aerosol Types Observed in Worldwide Locations, J. Atmos. Sci., 59(3), 590–608, doi:10.1175/1520-0469(2002)059<0590:VOAAOP>2.0.CO;2, 2002.

Dubovik, O., Holben, B. N., Kaufman, Y. J., Yamasoe, M., Smirnov, A., Tanré, D. and Slutsker, I.: Single-scattering albedo

425   of smoke retrieved from the sky radiance and solar transmittance measured from ground, J. Geophys. Res., 103, 31903–31923, doi:10.1029/98JD02276, 1998.

Dubovik, O. and King, M. D.: A flexible inversion algorithm for retrieval of aerosol optical properties from Sun and sky radiance measurements, J. Geophys. Res., 105, 20637–20969, doi:10.1029/2000JD900282, 2000.

Dubovik, O., Smirnov, A., Holben, B. N., King, M. D., Kaufman, Y. J., Eck, T. F. and Slutsker, I.: Accuracy assessments of

430   aerosol optical properties retrieved from Aerosol Robotic Network (AERONET) Sun and sky radiance measurements, J. Geophys. Res., 105, 9791–9806, doi:10.1029/2000JD900040, 2000.

Eck, T. F., Holben, B. N., Ward, D. E., Mukelabai, M. M., Dubovik, O., Smirnov, A., Schafer, J. S., Hsu, N. C., Piketh, S. J., Queface, A., Roux, J. Le, Swap, R. J. and Slutsker, I.: Variability of biomass burning aerosol optical characteristics in southern Africa during the SAFARI 2000 dry season campaign and a comparison of single scattering albedo estimates from

435   radiometric measurements, J. Geophys. Res., 108, 8477, doi:10.1029/2002JD002321, 2003.

Eck, T. F., Holben, B. N., Reid, J. S., Mukelabai, M. M., Piketh, S. J., Torres, O., Jethva, H. T., Hyer, E. J., Ward, D. E.,

Dubovik, O., Sinyuk, A., Schafer, J. S., Giles, D. M., Sorokin, M., Smirnov, A. and Slutsker, I.: A seasonal trend of single scattering albedo in southern African biomass-burning particles : Implications for satellite products and estimates of emissions for the world ' s largest biomass-burning source, J. Geophys. Res., 118, 6414–6432, doi:10.1002/jgrd.50500,

440   2013.

Gassó, S. and Torres, O.: The role of cloud contamination, aerosol layer height and aerosol model in the assessment of the OMI near-UV retrievals over the ocean, Atmos. Meas. Tech., 9(7), 3031–3052, doi:10.5194/amt-9-3031-2016, 2016.

Satheesh, S. K., Torres, O., Remer, L. A., Babu, S. S., Vinoj, V., Eck, T. F., Kleidman, R. G. and Holben, B. N.: Improved assessment of aerosol absorption using OMI-MODIS joint retrieval, J. Geophys. Res. Atmos., 114(5), 1–10,

445   doi:10.1029/2008JD011024, 2009.

Ginoux, P., Prospero, J. M., Torres, O. and Chin, M.: Long-term simulation of global dust distribution with the GOCART model: Correlation with North Atlantic Oscillation, Environ. Model. Softw., 19, 113–128, doi:10.1016/S1364-8152(03)00114-2, 2004.

Herman, J. R., Bhartia, P. K., Torres, O., Hsu, C., Seftor, C. and Celarier, E.: Global distribution of UV-absorbing aerosols

450   from Nimbus 7/TOMS data, J. Geophys. Res., 102, 16911–16992, doi:10.1029/96JD03680, 1997.

Holben, B. N., Eck, T. F., Slutsker, I., Smirnov, A., Sinyuk, A., Schafer, J., Giles, D., Dubovik, O. and Lille, U. S. T. De: AERONET's Version 2 .0 quality assurance criteria, Int. Soc. Opt. Photonics, 6408, 64080Q, 2006.

Hsu, N. C., Tsay, S. C., King, M. D. and Herman, J. R.: Aerosol properties over bright-reflecting source regions, IEEE Trans. Geosci. Remote Sens., 42, 557–569, doi:10.1109/TGRS.2004.824067, 2004.

455   Hu, R. M., Martin, R. V. and Fairlie, T. D.: Global retrieval of columnar aerosol single scattering albedo from space-based observations, J. Geophys. Res. Atmos., 112, D02204, doi:10.1029/2005JD006832, 2007.

IPCC, 2007: Climate Change 2007: Synthesis Report. Contribution of Working Groups I, II and III to the Fourth Assessment Report of the Intergovernmental Panel on Climate Change [Core Writing Team, Pachauri, R.K and Reisinger, A. (eds.)]. IPCC, Geneva, Switzerland, 104 pp.

460   IPCC, 2014: Climate Change 2014: Synthesis Report. Contribution of Working Groups I, II and III to the Fifth Assessment Report of the Intergovernmental Panel on Climate Change [Core Writing Team, R.K. Pachauri and L.A. Meyer (eds.)]. IPCC, Geneva, Switzerland, 151 pp.

Jethva, H., Torres, O., Sciences, P. and Space, G.: Satellite-based evidence of wavelength-dependent aerosol absorption in biomass burning smoke inferred from Ozone Monitoring Instrument, , 10541–10551, doi:10.5194/acp-11-10541-2011, 2011.

465   Kaskaoutis, D.G.; Nastos, P.T.; Kosmopoulos, P.G.; Kambezidis, H.D.; Kharol, S.K.and Badarinath, K. V. S.: The Aura – OMI Aerosol Index distribution over Greece, Atmos. Res. J., 98, 28–39, doi:10.1016/j.atmosres.2010.03.018, 2010.

Kassianov, E. I., Barnard, J. C. and Ackerman, T. P.: Retrieval of aerosol microphysical properties using surface MultiFilter Rotating Shadowband Radiometer (MFRSR) data : Modeling and observations, J. Geophys. Res., 110, D09201, doi:10.1029/2004JD005337, 2005.

470   Kaufman, Y. J., Tanré, D. and Boucher, O.: A Satellite View of Aerosols in the Climate System, Nature, 419, 215–223, 2002.

Koch, D. and Del Genio, A. D.: Black carbon semi-direct effects on cloud cover: Review and synthesis, Atmos. Chem. Phys., 10, 7685–7696, doi:10.5194/acp-10-7685-2010, 2010.

Lee, K. H., Li, Z., Kim, Y. J. and Kokhanovsky, A.: Atmospheric Aerosol Monitoring fromSatellite Observations: A History

475   of Three Decades, in Atmospheric and Biological Environmental Monitoring, pp. 13–38., 2009.

Leroy, M., Deuzé, J. L., Bréon, F. M., Hautecoeur, O., Herman, M., Buriez, J. C., Tanré, D., Bouffiès, S., Chazette, P. and Roujean, J. L.: Retrieval of atmospheric properties and surface bidirectional reflectances over land from POLDER/ADEOS, J. Geophys. Res., 102, 17023-17037, doi:10.1029/96JD02662, 1997.

Levelt, P. F., Oord, G. H. J. Van Den, Dobber, M. R., Mälkki, A., Visser, H., Vries, J. De, Stammes, P., Lundell, J. O. V and

480 Saari, H.: The Ozone Monitoring Instrument, IEEE Trans. Geosci. Remote Sens., 44, 1093–1101, 2006.\

Myhre, G., Shindell, D., Bréon, F. M., Collins, W., Fuglestvedt, J., Huang, J., ... & Nakajima, T.: Anthropogenic and Natural Radiative Forcing, Clim. Chang., 432, 658–740, 2013.

Nakajima, T., Tanaka, M. and Yamauchi, T.: Retrieval of the optical properties of aerosols from aureole and extinction data, Appl. Opt., 22, 2951–2959, 1983.

485 Nakajima, T., Tonna, G., Rao, R., Boi, P., Kaufman, Y. and Holben, B.: Use of sky brightness measurements from ground for remote sensing of particulate polydispersions, Appl. Opt., 35, 2672–2686, doi:10.1364/AO.35.002672, 1996.

NASA.gov: NASA's Terra Catches Fires in Central Chile, [online] Available from: https://www.nasa.gov/image-feature/goddard/2017/nasas-terra-catches-fires-in-central-chile (Accessed 1 May 2017), 2017.

Petters, J. L., Saxena, V. K., Slusser, J. R., Wenny, B. N. and Madronich, S.: Aerosol single scattering albedo retrieved from

490 measurements of surface UV irradiance and a radiative transfer model, J. Geophys. Res., 108, 4288, doi:10.1029/2002JD002360, 2003.

Ramanathan, V. and Carmichael, G.: Global and regional climate changes due to black carbon, Nat. Geosci., 1, 221–227, doi:10.1038/ngeo156, 2008.

Reid, J. S., Eck, T. F., Christopher, S. A., Koppmann, R., Dubovik, O., Eleuterio, D. P., Holben, B. N., Reid, E. A. and

495 Zhang, J.: A review of biomass burning emissions part III: intensive optical properties of biomass burning particles, Atmos. Chem. Phys. Discuss., doi:10.5194/acpd-4-5201-2004, 2004.

Remer, L.A., Kaufman; Y.J., Tanré; D., Mattoo, S., Chu, D.A., Martins, J.V., Li, R.R., Ichiku, C., Levy, R.C., Kleidman, R.G., Eck, T.K., Vermote, E. and Holben, B. N.: The MODIS Aerosol Algorithm, Products, and Validation, J. Atmos. Sci., 62, 947–973, 2005.

500 Remer, L.A., Tanré, D. and Kaufman, Y. J.: Algorithm for remote sensing of tropospheric aerosol from MODIS:Collection 5 Product ID: MOD04/MYD04-C005., 1998.

Sanders, A.F.J. and de Haan, J.F: TROPOMI ATBD of the Aerosol Layer Height product, 2016.
Stein Zweers, D.C: TROPOMI ATBD of the UV aerosol index., 2016.

Satheesh, S. K., Torres, O., Remer, L. A., Babu, S. S., Vinoj, V., Eck, T. F., Kleidman, R. G. and Holben, B. N.: Improved

505 assessment of aerosol absorption using OMI-MODIS joint retrieval, J. Geophys. Res. Atmos., 114(5), 1–10, doi:10.1029/2008JD011024, 2009.

Tanr, D., J Kaufman, B. Y., Herman, M. and Mattoo, S.: Remote sensing of aerosol properties over oceans using the MODIS/EOS spectral radiances, J. Geophys. Res., 102, 16971–16988, doi:10.1029/96JD03437, 1997.

The Guardian: Chile battles devastating wildfires: 'We have never seen anything on this scale', [online] Available from:

510 https://www.theguardian.com/world/2017/jan/25/chile-fire-firefighting-international-help?utm_source=Climate+News+Network&utm_campaign=afdf3cf10c-EMAIL_CAMPAIGN_2017_02_03&utm_medium=email&utm_term=0_1198ea8936-afdf3cf10c-38798061 (Accessed 25 Jan 2017), 2017.

Torres, O., Bhartia, P. K., Herman, J. R., Ahmad, Z. and Gleason, J.: Derivation of aerosol properties from satellite

515 measurements of backscattered ultraviolet radiation: Theoretical basis, J. Geophys. Res. Atmos., 103, 17099–17110, doi:10.1029/98JD00900, 1998.

Torres, O., Bhartia, P. K., Sinyuk, A., Welton, E. J. and Holben, B.: Total Ozone Mapping Spectrometer measurements of aerosol absorption from space: Comparison to SAFARI 2000 ground-based observations, J. Geophys. Res. D Atmos., 110, D10S18, doi:10.1029/2004JD004611, 2005.

520 Torres, O., Tanskanen, A., Veihelmann, B., Ahn, C., Braak, R., Bhartia, P. K., Veefkind, P. and Levelt, P.: Aerosols and surface UV products from Ozone Monitoring Instrument observations : An overview, J. Geophys. Res., 112, D24S47, doi:10.1029/2007JD008809, 2007.

Torres, O., Jethva, H. and Bhartia, P. K.: Retrieval of Aerosol Optical Depth above Clouds from OMI Observations: Sensitivity Analysis and Case Studies, J. Atmos. Sci., 69, 1037–1053, doi:10.1175/JAS-D-11-0130.1, 2012.

525 Tukey, J.W.: Exploratory data analysis, Addison-Wesley Publishing Company, 1977.

Winker, D. M., Vaughan, M. A., Omar, A., Hu, Y., Powell, K. A., Liu, Z.;Hunt, W.H.;Young, S. A.: Overview of the CALIPSO Mission and CALIOP Data Processing Algorithms, Technol. J. Atmos. Ocean., 26, 2310–2323, doi:10.1175/2009JTECHA1281.1, 2009.

Yin, B., Min, Q. and Joseph, E.: Retrievals and uncertainty analysis of aerosol single scattering albedo from MFRSR

530 measurements, J. Quant. Spectrosc. Radiat. Transf., 150, 95–106, doi:10.1016/j.jqsrt.2014.08.012, 2015.

535

540

545

550
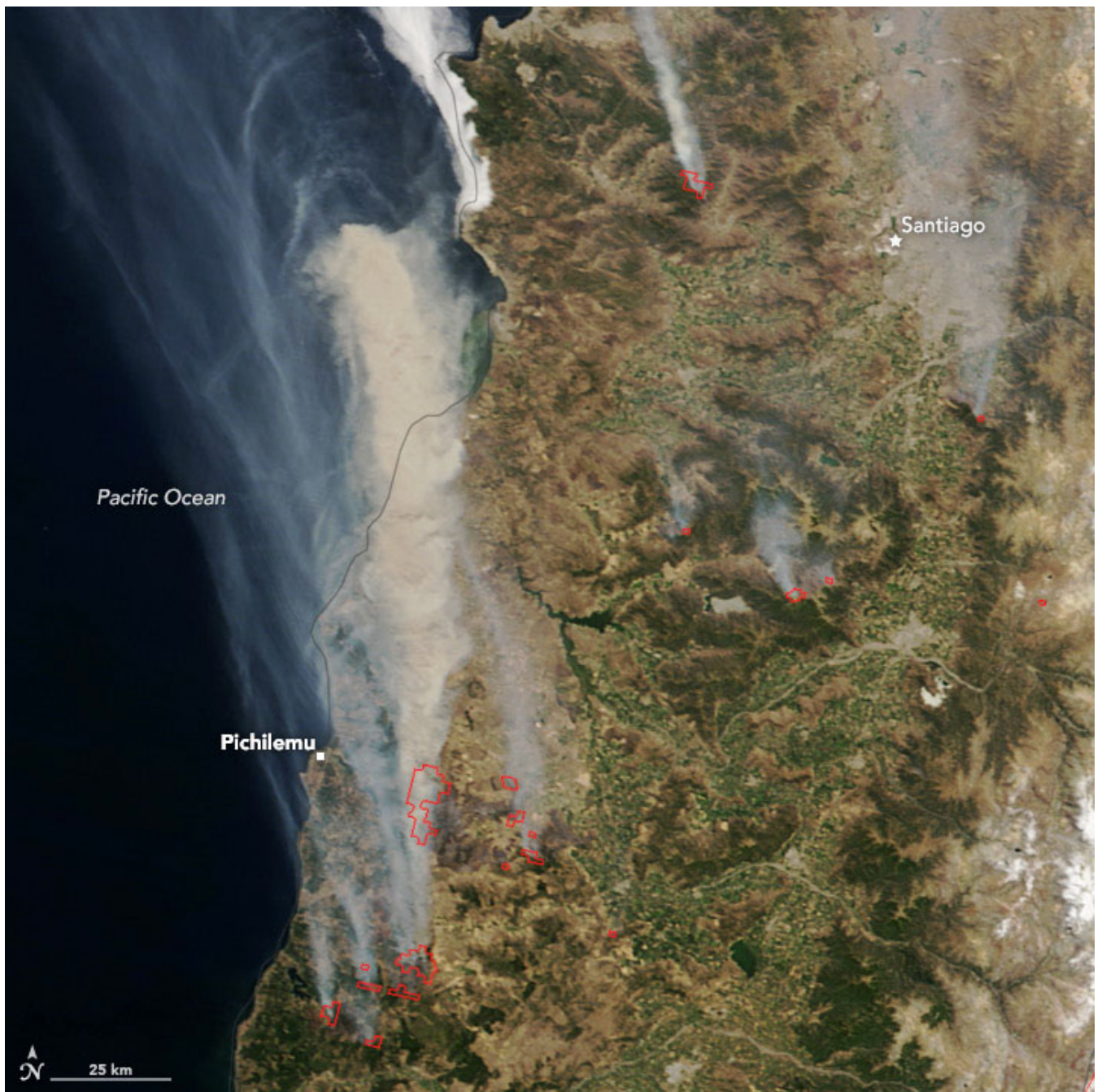
555 **Figure 1: Chile wildfires detected by Terra/MODIS on 20 January 2017 (Image source: NASA's Earth Observatory https://earthobservatory.nasa.gov/IOTD/view.php?id=89496).**

560

565

570
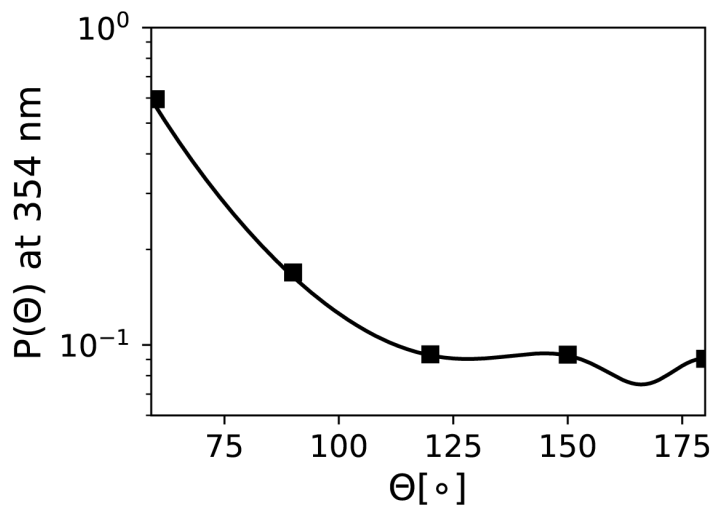
Figure 2: Phase function p(Θ) at 354 nm of the parameterized Mie scattering aerosols in sensitivity analysis. The markers in the plot correspond to the value when Θ=60°, 90°, 120°, 150°, 180°.

575

580

585

590
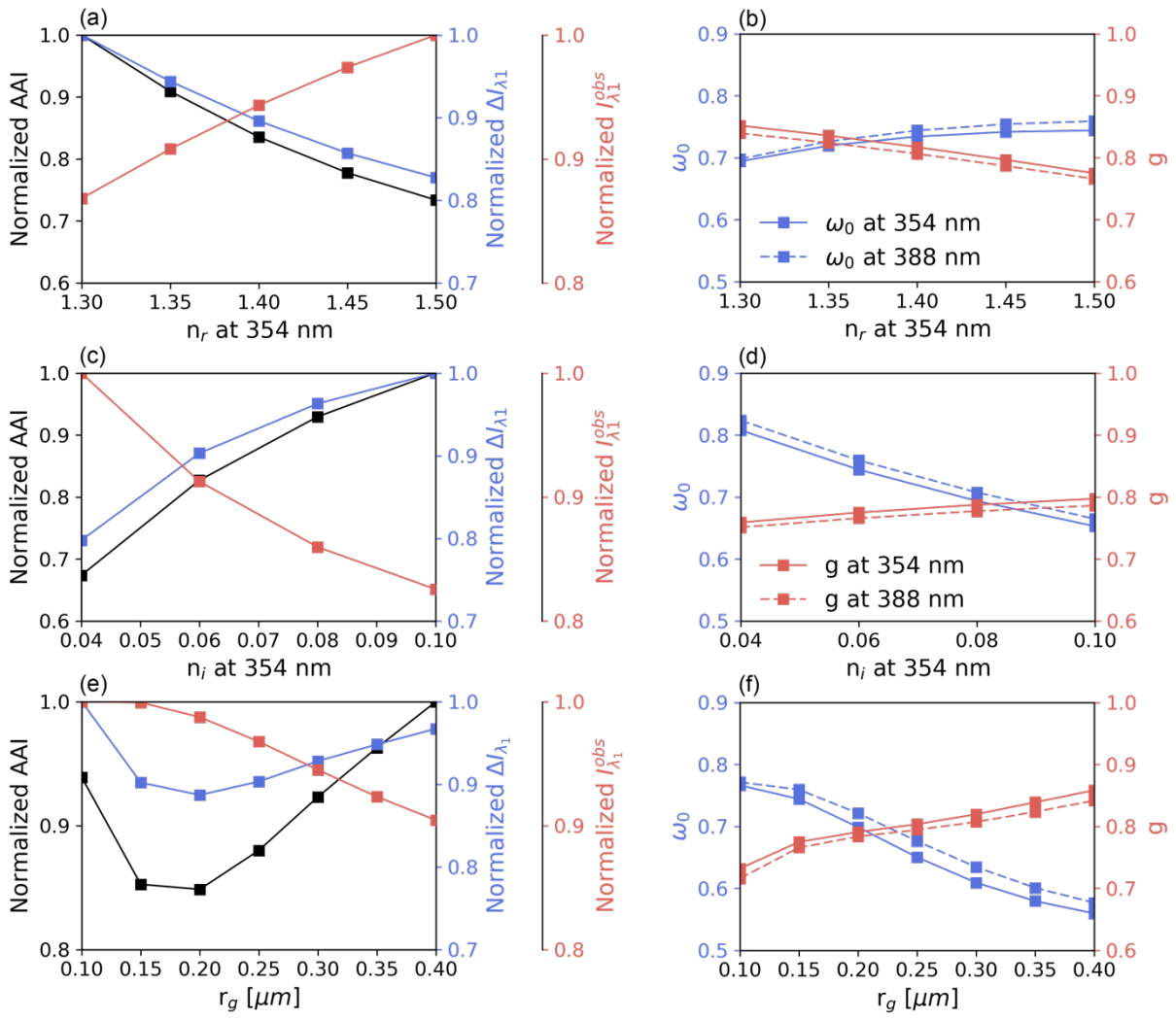
Figure 3: AAI sensitivity to micro-physical parameters: n_i (a, b), n_r (c, d), and r_g (e, f). The left panels (a, c and e) show the sensitivity of the normalized AAI (black), the normalized $\Delta I_{\lambda 1}$ (blue) and the normalized $I_{\lambda 1}^{obs}$ (red). The right panels (b, d and f) show ω_0 (blue) and g (red) at wavelength 354 (solid line) and 388 (dashed line) nm, respectively.

595
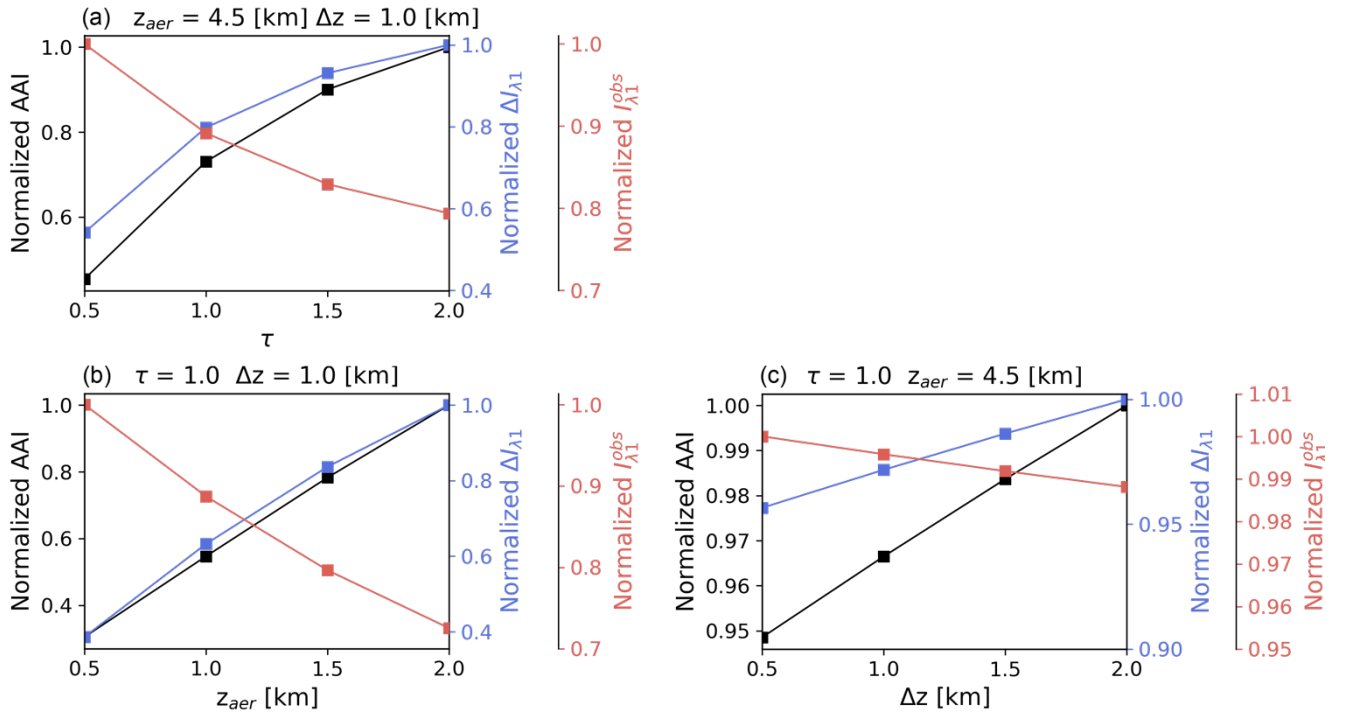
Figure 4: AAI sensitivity to macro-physical parameters: (a) τ at 550 nm, (b) z_{aer} and (c) Δz.

600

605

610
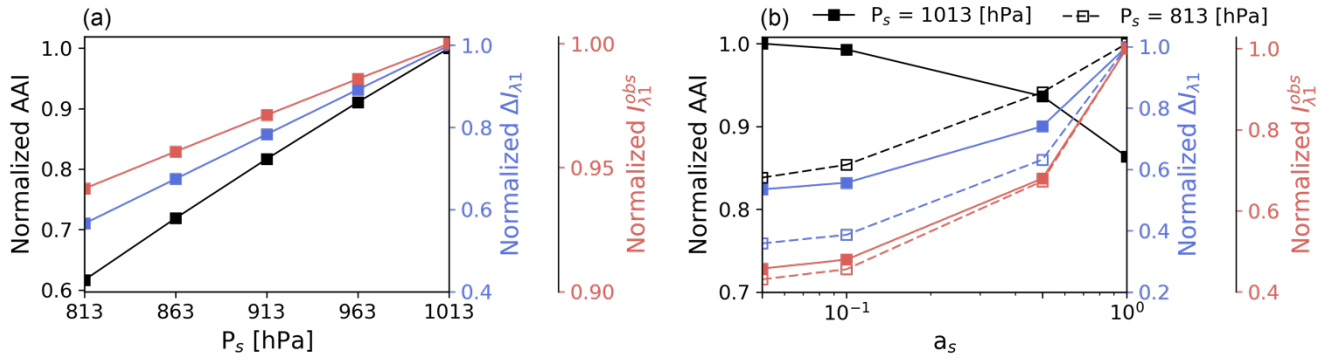
Figure.5 AAI sensitivity to surface parameters: a_s(a) and P_s(b). The solid line and dashed line in (b) indicates terrain height at sea level (P_s = 1013 hPa) and elevated terrain height (P_s = 813 hPa), respectively.

615

620

625

630

635

640
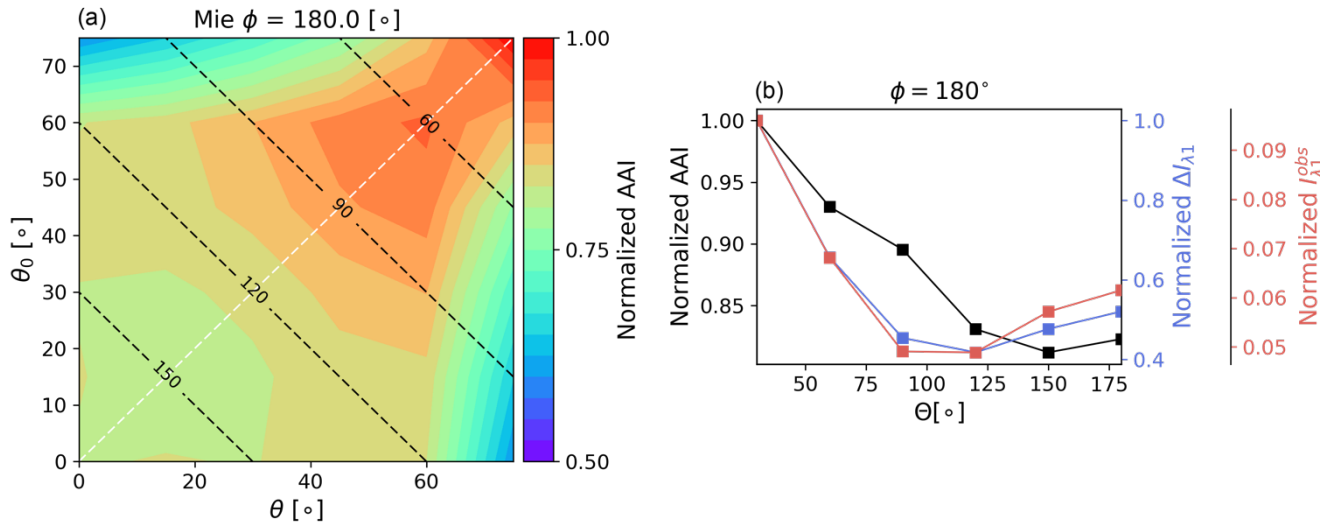
Figure.6 AAI sensitivity to θ and θ₀ at φ=180°. The black dashed contour in (a) indicates the Θ=60°, 90°, 120°, 150°. The white dashed line in (a) indicates the cross section.

665
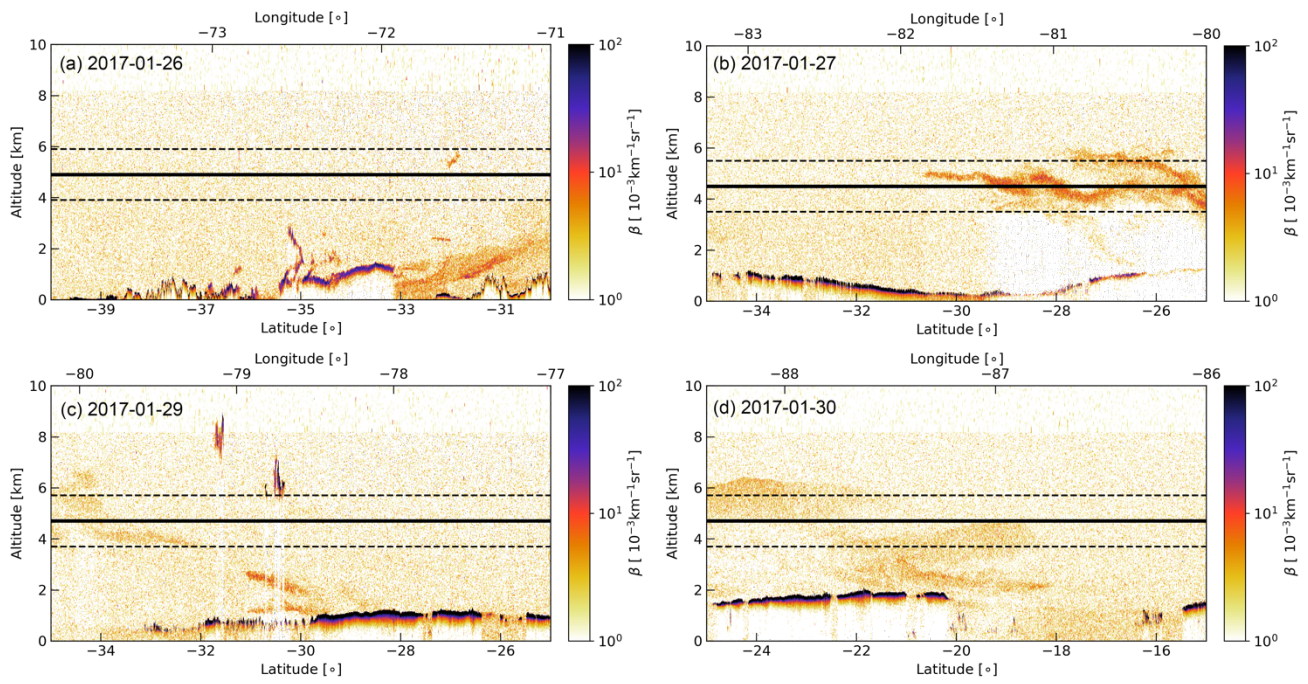
Figure.7 CALIOP backscatter coefficient β at 532 nm. The solid and dashed line indicate the retrieved z_{aer} and Δz, respectively.

670
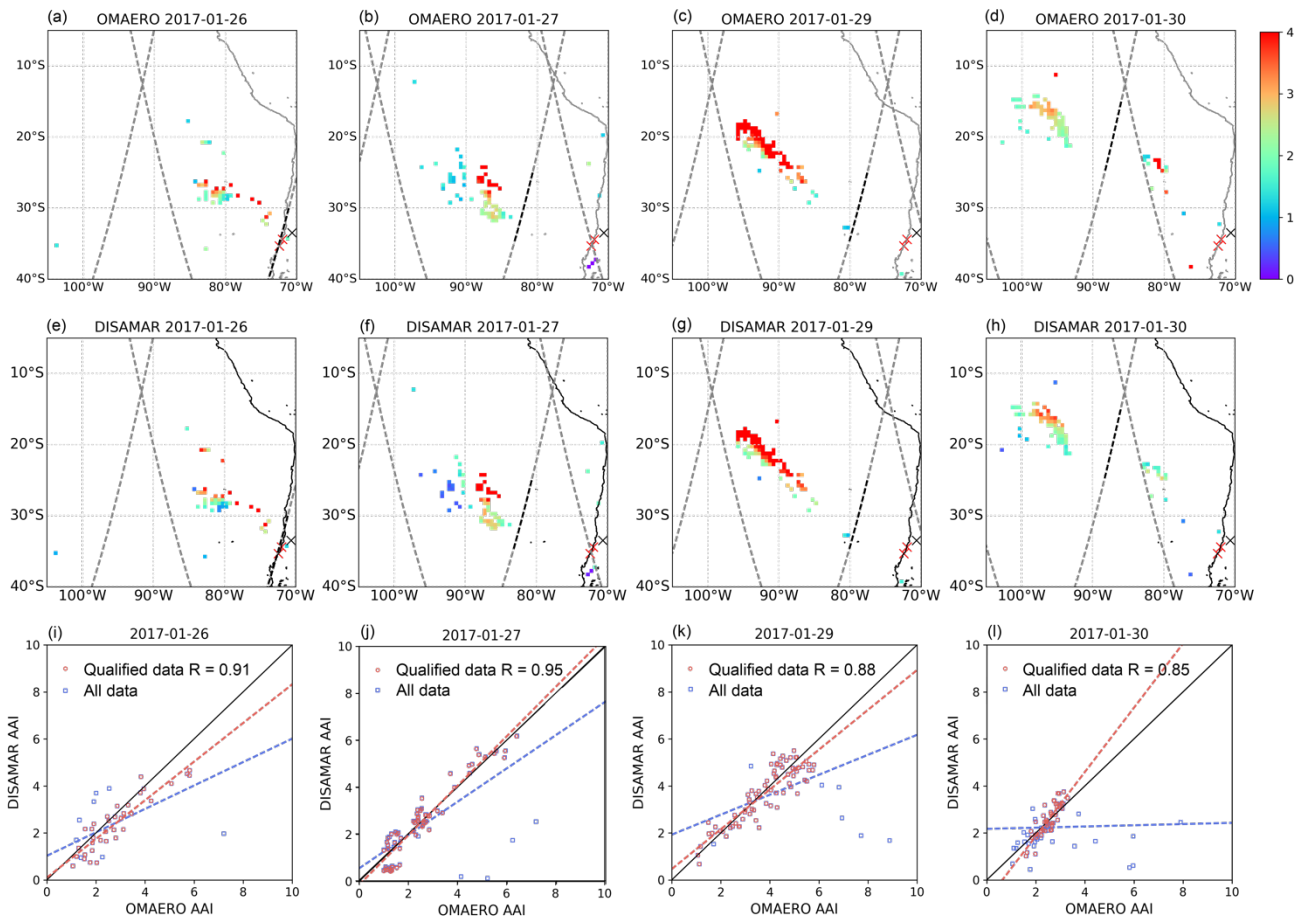
Figure.8 OMI observations (a–d) and DISAMAR simulations (e–h) of the Chile wildfires on 26, 27, 29 and 30 January 2017. The black and red cross symbols are the AERONET station and the main fire sources (Pichilemu W34.39˚ S72.00˚ and Consititución S35.33˚, W72.42˚), respectively. The grey dashed line indicates the CALIOP paths in the region of interest, where the paths used to validate the plume height are marked by black dashed line. The scatter plots (i–l) present the OMI observations against DISAMAR simulations for only qualified data (red dot) and all data (blue dot), respectively.
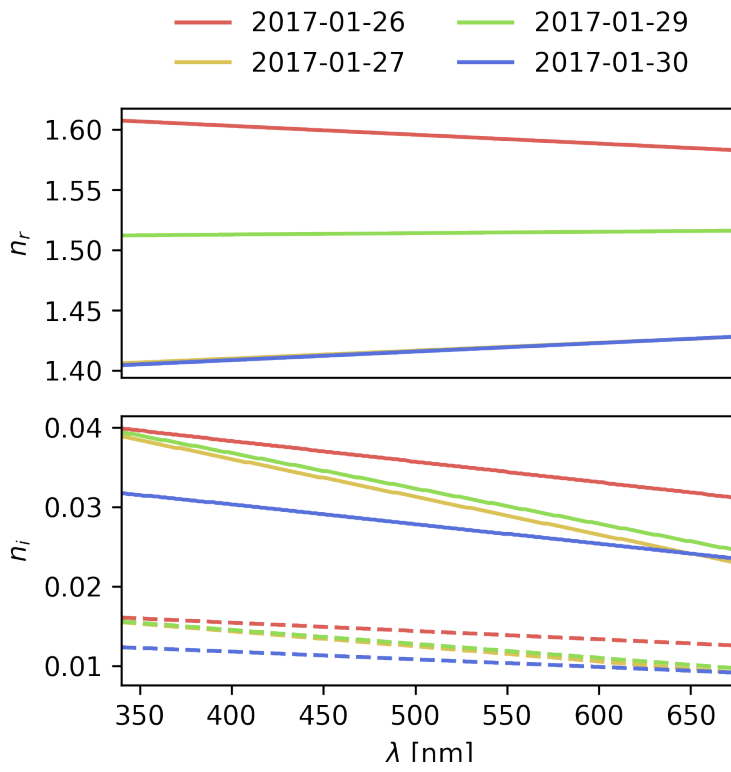
700 **Figure.9 Retrieved complex refractive index for each case. The dashed line in lower panel is the wavelength dependent imaginary refractive index (n_i) measured by AERONET.**

705

710
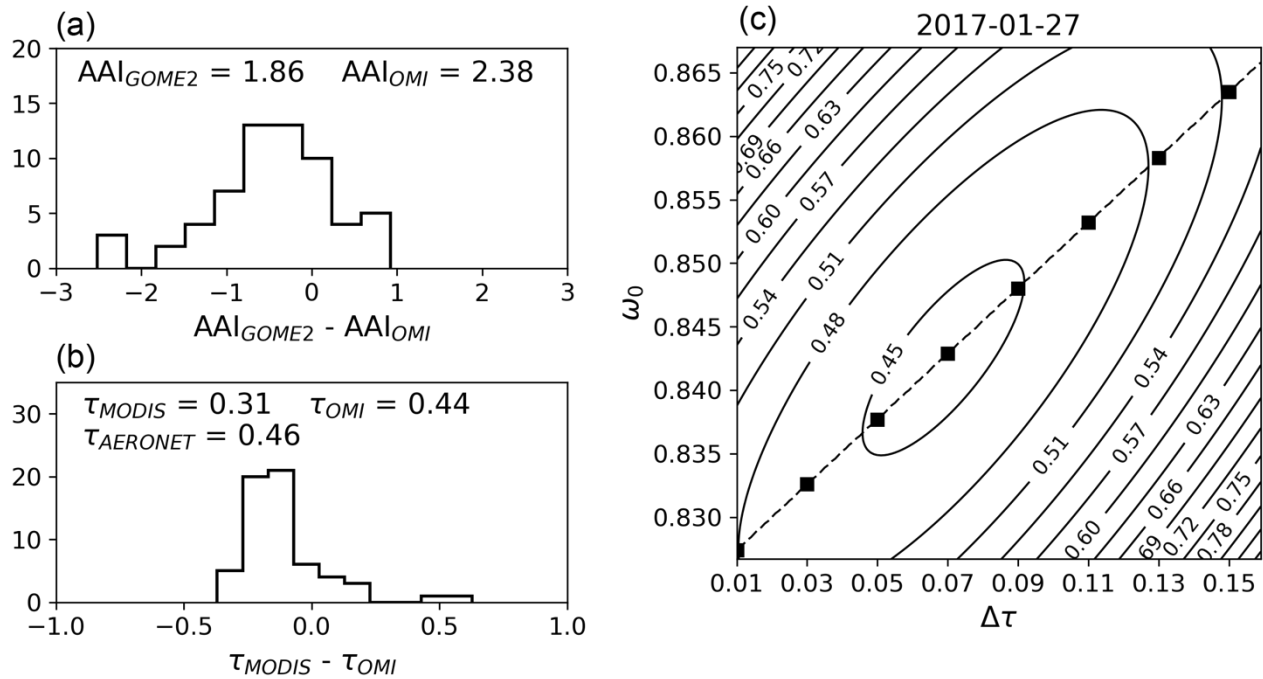
Figure.10 Histogram of (a) the AAI difference between GOME-2 and OMI, against (b) the τ difference at 550 nm between MODIS and OMI for 27 January. Contour of (c) the AAI RMSE as a function of variation in τ and ω₀ for 27 January. The dashed line is the best estimation for each pair of Δτ and ω₀.

715

720

725

730

735

Table 1. Parameters used in sensitivity analysis.

Parameters	Default value	Sensitivity range	Unit
Geometric mean radius (r_g)	0.15	0.1, 0.15, 0.2, 0.25, 0.3, 0.35, 0.4	μm
Geometric standard deviation (σ_g)	1.5	-	μm
Real refractive index (n_r) at 354 nm	1.5	1.3, 1.35, 1.4, 1.45, 1.5	-
Imaginary refractive index (n_i) at 354 nm	0.06	0.04, 0.06, 0.08, 0.1	-
Aerosol layer geometric central height (z_{aer})	4.5	2.5, 4.5, 6.5, 8.5	km
Aerosol layer geometric thickness(Δz)	1	0.5, 1, 1.5, 2	km
Aerosol optical thickness (τ) at 550 nm	1	0.5, 1, 1.5, 2	-
Surface albedo (a_s)	0.05	0.05, 0.1, 0.5, 1.0	-
Surface pressure (P_s)	1013	1013, 963, 913, 863, 813	hPa
Solar zenith angle (θ_0)	30	0, 15, 30, 45, 60, 75	°
Viewing zenith angle (θ)	0	0, 15, 30, 45, 60, 75	°
Relative azimuth angle ($\Delta\varphi = \varphi - \varphi_0 + 180°$)	0	0, ±45, ±90, ±135, ±180	°

740

745

750

755

760

765

Table.2 Summary of retrieved results (applying IQR outlier detection).

	Date	2017-01-26	2017-01-27	2017-01-29	2017-01-30
AAI	AAI median (OMAERO)	2.52	2.38	4.05	2.61
	AAI median (DISAMAR)	2.17	2.48	3.81	2.49
	Relative difference (%)	-13.88	4.20	-5.93	-4.60
	RMSE	0.67	0.51	0.60	0.41
Aerosol profile	z_{aer} [km]	4.9	4.5	4.7	4.7
	Δz [km]	2			
n_i	n_i at 354 nm	0.0395	0.0382	0.0388	0.0314
	n_i at 388 nm	0.0386	0.0366	0.0373	0.0306
	N_i difference between 354 and 388 nm	2.33%	4.37%	4.02%	2.61%
ω_0 at 550 nm	ω_0 (AERONET)	0.89	0.89	0.92	0.91
	ω_0 (DISAMAR)	0.83	0.81	0.87	0.85
	Relative difference (%)	-6.74	-8.99	-5.43	-6.59

770

775

780

785

790

795